PNAS RESEARCH ARTICLE | PHYSICS

Measurement of the dynamic charge susceptibility near the charge density wave transition in $ErTe_3$

Dipanjan Chaudhuri[a,b,1], Qianni Jiang[c], Xuefei Guo[a,b], Jin Chen[a,b], Caitlin S. Kengle[a,b], Farzaneh Hoveyda-Marashi[a,b], Camille Bernal-Choban[a,b], Niels de Vries[a,b], Tai-Chang Chiang[a,b], Eduardo Fradkin[a,d], Ian R. Fisher[c], and Peter Abbamonte[a,b,1]

Affiliations are included on p. 5.

Edited by J. C. Davis, University of Oxford, Oxford, United Kingdom; received November 29, 2024; accepted May 10, 2025

A charge density wave (CDW) is a phase of matter characterized by a periodic modulation of valence electron density coupled with lattice distortion. Its formation is closely tied to the dynamical charge susceptibility, $\chi(q,\omega)$, which reflects the collective electron dynamics of the material. Despite decades of study, $\chi(q,\omega)$ near a CDW transition has never been measured at nonzero momentum, q, with meV energy resolution. Here, we investigate the canonical CDW transition in $ErTe_3$ using momentum-resolved electron energy loss spectroscopy, a technique uniquely sensitive to valence band charge excitations. Unlike phonons, which soften via the Kohn anomaly, we find the electronic excitations exhibit purely relaxational dynamics well described by a diffusive model, with the diffusivity peaking just below the critical temperature, T_{C1}. Additionally, we report for the first time a divergence in the real part of $\chi(q,\omega)$ in the static limit ($\omega \to 0$), a long-predicted hallmark of CDWs. Unexpectedly, this divergence occurs as $T \to 0$, with only a weak thermodynamic signature at $T = T_{C1}$. Our study necessitates a reexamination of the traditional description of CDW formation in quantum materials.

charge density wave | charge susceptibility | M-EELS

Charge density waves (CDWs) are widespread in interacting electron materials and often coexist with other Fermi surface instabilities, such as magnetism or superconductivity (1). Initially proposed for one-dimensional systems, CDW ground states have been observed across a range of strongly correlated materials with varying dimensionalities, including cuprate high-temperature superconductors (2), transition metal chalcogenides (3), transition metal bronzes, and organic conductors (4), among others (5, 6). A deep understanding of the behavior and underlying mechanisms of CDWs is crucial for advancing the study of quantum materials.

An expected thermodynamic signature of the onset of a CDW phase is a divergence in static charge susceptibility $\chi(q)$, which favors a periodic redistribution of charge in the ordered state (1). This redistribution causes a gap to open in the single-particle density of states and is accompanied by a periodic distortion of the structural lattice driven by electron–phonon coupling. Although this phenomenon is most pronounced in one-dimensional systems where a Peierls instability due to Fermi surface nesting leads to logarithmic divergence (5), CDW phases have been widely observed in higher-dimensional systems in which nesting is imperfect and strongly dependent on the morphology of the Fermi surface (7, 8).

The precise microscopic mechanism driving CDW behavior in most materials remains elusive. The nesting picture by itself is usually too simplistic, and effects such as temperature, scattering, and band velocity mismatch at the nesting wave vector play a crucial role in real materials (8, 9). Correspondence between the CDW wave vector and the nesting properties of the Fermi surface is often difficult to discern (10). Other aspects, such as the momentum dependence of the electron–phonon interaction, have been invoked to quantitatively relate theory and experiments (7, 11–13). It is therefore crucial to experimentally measure the low-energy charge dynamics of a prototypical CDW material to understand the collective excitations that drive the CDW instability, and to determine whether, and how, a susceptibility divergence occurs.

Many of the essential properties of CDWs have been studied by a variety of experimental probes. The transport and thermodynamic anomalies associated with the CDW phase transition are widely observed in resistivity and specific heat measurements (5, 14–16), the periodic lattice distortion is measured with X-ray and neutron diffraction (5, 17–19), the CDW gap is probed through angle-resolved photoemission spectroscopy

Significance

A hallmark of a second-order phase transition is a divergent susceptibility of the associated order. The dynamics of the corresponding order parameter is encoded in the behavior of the susceptibility near the critical point. For a charge density wave (CDW) phase, characterized by the formation of a static charge modulation which spontaneously breaks the lattice translational symmetry, the relevant parameter is the dynamical charge susceptibility, $\chi(q,\omega)$. Yet, $\chi(q,\omega)$ has never been measured explicitly with adequate sensitivity and resolution, primarily due to a dearth of experimental probes capable of directly coupling to it. Studying the electronic response across a prototypical CDW transition is therefore of paramount importance for a holistic understanding of its microscopic origin and electrodynamic response.

Author contributions: D.C. led the M-EELS experiments and data analysis, with assistance from X.G., J.C., C.S.K., F.H.-M., C.B.-C., and N.V.; Q.J. and I.R.F. grew and characterized the ErTe3 single crystal samples; T.-C.C. and E.F. provided theoretical support; P.A. directed the project. D.C. and P.A. wrote the paper with input from all authors.

The authors declare no competing interest.

This article is a PNAS Direct Submission.

[1]To whom correspondence may be addressed. Email: dc36@illinois.edu or abbamont@illinois.edu.

This article contains supporting information online at https://www.pnas.org/lookup/suppl/doi:10.1073/pnas.2424430122/-/DCSupplemental.

Published June 20, 2025.

(ARPES) (10, 20, 21) and optical spectroscopy (22–24), and the soft phonon collective mode of CDWs have been observed with inelastic X-ray (25–27) and neutron scattering experiments (28, 29).

The behavior of the charge susceptibility itself, however, has never been measured. The reason is a shortage of experimental probes that measure the charge response at nonzero momentum, q, with meV energy resolution. Inelastic neutron scattering, for example, couples to matter through the nuclei or electron spins, so is only sensitive to phonons and spin excitations (30, 31). As explained in *SI Appendix*, inelastic X-ray scattering (IXS) is also mainly sensitive to phonon excitations, since X-rays couple to the electron density and phonons modulate the location of the atomic cores, where most of the electrons reside (32, 33). Previous attempts to estimate the momentum-resolved dynamic charge susceptibility therefore had to rely on computing the Lindhard response by parameterizing the experimental band structure obtained from ARPES measurements, which neglect excitonic effects, vertex corrections, and other many-body phenomena (8, 33, 34). A measurement sensitive to the electronic susceptibility near a CDW transition is therefore still lacking.

Here, we present measurements of the charge susceptibility of the prototypical CDW material $ErTe_3$ with momentum-resolved electron energy loss spectroscopy (M-EELS). Electrons couple to the *charge* density, so the scattering cross-section directly measures the dynamic charge susceptibility of the surface,

$$\chi_S''(q,\omega) = \int_{-\infty}^{0} dz_1 dz_2 \chi''(q,\omega,z_1,z_2) e^{-|\mathbf{q}||z_1+z_2|}, \qquad [1]$$

where $\chi''(q,\omega,z_1,z_2)$ is the bulk susceptibility and the in-plane momentum, q, can range over multiple Brillouin zones (see refs. 32, 33, and 35 and *SI Appendix*). Eq. **1** indicates that the probe depth of M-EELS is given by the inverse of the in-plane momentum transfer, q, making it more bulk sensitive than true surface spectroscopies such as ARPES and scanning tunneling microscopy (STM) (32, 33).

The current measurements were performed with an energy resolution of ≈5.6 meV (FWHM), which is sufficient to observe the low-energy charge excitations due to electrons near the Fermi surface involved in CDW formation. M-EELS has previously been successfully applied to valence band charge excitations in Bi_2Se_3 (36), $TiSe_2$ (37), $Bi_2Sr_2CaCu_2O_{8+x}$ (38, 39), ZrSiS (40), Sr_2RuO_4 (41), and $SrTiO_3$ (42). M-EELS is therefore an ideal probe for investigating the charge susceptibility near a CDW transition.

The family of rare-earth tritellurides, RTe_3 (R = La, Ce, Pr, Sm, Gd-Tm), are canonical quasi-2D CDW materials (16, 19, 43). They have a weakly orthorhombic crystal structure consisting of bilayer, nominally square Te nets along the *ac* planes that are separated by corrugated RTe slabs stacked along *b*-axis (Fig. 1*A*). The precise CDW transition temperature depends on the chemical pressure exerted by the rare-earth atom. A second CDW, with lower transition temperature and a modulation orthogonal to the first, is observed when the rare-earth element is heavier than Dy (19). Transport and X-ray diffraction studies have found that the CDWs in all these materials are incommensurate (19). While phonon softening was observed in the vicinity of the CDW ordering wave vector (25, 26), the electronic excitations associated with the transition have not been studied.

$ErTe_3$ is a representative of the series with two CDW transitions, at $T_{C1} \approx 267$ K and $T_{C2} \approx 159$ K with $q_{C1} \approx (5/7)\,c^*$ and $q_{C2} \approx (2/3)\,a^*$ respectively (19). ARPES studies at low temperatures revealed a large gap at the Fermi surface, $\Delta_1 \approx 175$ meV along c^*, and a smaller gap, $\Delta_2 \approx 50$ meV was along a^* (20) (Fig. 1*B*). The magnitudes of these gaps are consistent with infrared spectroscopy (22). While X-ray diffraction (19) and ARPES measurements (20) were initially interpreted in terms of Fermi surface nesting alone (45), detailed numerical simulations (8) along with Raman (12), and inelastic X-ray scattering (25) studies have emphasized the importance of strongly momentum-dependent electron–phonon coupling in determining the CDW wave vector. The second, lower temperature CDW in the RTe_3 family is generally believed to be more subtle, since it does not show any signatures of phonon softening near the transition (26). We therefore focus our attention here on the higher transition in $ErTe_3$, which should serve as a canonical example of a CDW that exemplifies the behavior of the dynamic charge response at such a transition.

Single crystal samples of $ErTe_3$, grown using the self-flux method (16), were cleaved perpendicular to the *b*-axis in ultra-high vacuum prior to the M-EELS measurement. The cleaved samples were orientated such that the 50 eV incident electrons were scattered off along *bc* plane with the in-plane momentum transfer, q, along the c axis (Fig. 1*C*).

Elastic scattering from the CDW (energy loss $\hbar\omega \approx 0$), plotted as a function of q for several temperatures in the vicinity of T_{C1}, is shown in Fig. 2*A*. Both the $(H, L) = (0, 1)$ crystalline Bragg peak and the CDW satellite at $(H, L) \sim (0, 0.7)$ are visible in the scans. The width of the (0,1) Bragg peak is a measure of the overall momentum resolution of the experiment, which is better than 0.01 r.l.u. (*SI Appendix*).

The lineshape of a CDW momentum spectrum is known to be highly sensitive to disorder (5). In the absence of disorder, the momentum spectrum of a CDW should have a power-law lineshape above its transition temperature, because of critical fluctuations near the transition, and become resolution-limited below the transition (1, 46). In the presence of disorder, however, a CDW can never exhibit true, long-ranged order in $d < 4$ (47). Nie and coworkers (48, 49) argued that, under such circumstances, the equal-time correlation function should instead be the sum of two terms,

$$S(Q,T) = \sigma^2 G^2(Q,T) + TG(Q,T), \qquad [2]$$

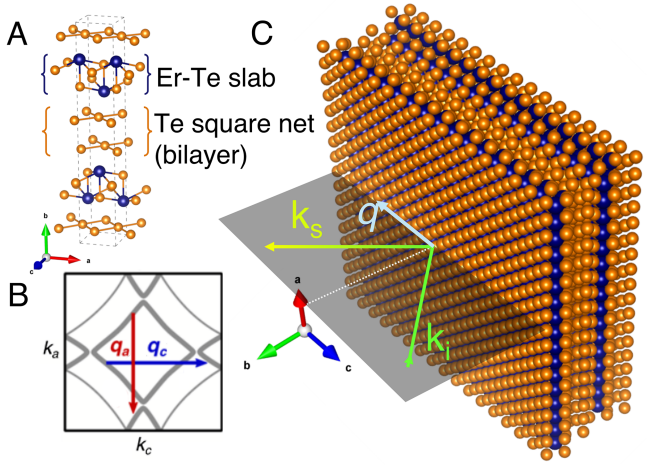

Fig. 1. (*A*) Crystal structure of $ErTe_3$ showing the corrugated Er-Te slabs and Te square nets. (*B*) Schematic of the Fermi surface showing the nesting vectors (adapted from ref. 44). (*C*) Scattering geometry of the experiment with reference to the sample orientation. k_i and k_s represent momenta of the incident and scattered electron, respectively, and q is the in-plane momentum transfer which is along the *c*-axis.

where $G(Q, T) = 1/[\kappa Q^2 + \mu(T)]$ is a Lorentzian, σ represents the disorder strength, $Q = q - q_0$ is the momentum relative to the CDW wave vector, and the other parameters quantify the CDW stiffness and correlation length. The first term in Eq. **2** is truly static, while the second is dynamical and, in principle, could be eliminated by using an energy analyzer that perfectly isolates the elastic ($\omega = 0$) response.

We found that the lineshape of the CDW momentum spectrum in $ErTe_3$ fit best to the single-Lorentzian expression,

$$I(q, T) = \frac{A(T)}{(q - q_0(T))^2 + \gamma_q^2(T)} + m(T)q + c(T), \quad [3]$$

where $q_0(T)$ is the CDW ordering wave vector and the width, $\gamma_q(T)$, is proportional to the inverse correlation length (*SI Appendix*). The sum $m(T)q + c(T)$ represents a linear background whose meaning will be discussed further below. Surprisingly, adding an additional, Lorentzian-squared term did not improve the quality of the fits. This is surprising given that our measurement is energy-resolved, with an overall resolution of 5.6 meV, and should isolate the Lorentzian-squared term in Eq. **2**. We conclude that the CDW in $ErTe_3$ is influenced by disorder, but extremely weakly.

The integrated intensity of the elastic CDW reflection, $I_{CDW}(T)$, is plotted in Fig. 2*B*. $I_{CDW}(T)$ is proportional to the square of the order parameter, $\Delta(T)$, and a fit to the BCS interpolation formula $\Delta(T) = \Delta_0 \tanh\left(1.74\sqrt{T_c/T - 1}\right)$, yields a $T_C = 268(7)K$ which is consistent with the previous X-ray diffraction measurements (19). In the intermediate regime between 100 to 250 K, the integrated intensity is smaller than the mean field prediction, which was also observed in the evolution of the single-particle gap in ARPES (20). Vestiges of the CDW order are also observed above T_c, up to $T = 290$ K, presumably due to pinning on disorder (5).

Fig. 2*C* shows the ratio of the width of the CDW to that of the (0,1) Bragg peak, i.e., $w(t) = \gamma_{CDW}/\gamma_{(0,1)}$, as a function of temperature. Below, 225 K the width of the CDW is nearly the same as that of the Bragg peak, indicating that it is limited by the instrumental resolution. This further supports the conclusion that disorder plays little role in the properties of this CDW. Above 225 K, the CDW peak broadens, indicating that the CDW correlation length gets shorter as the temperature is increased through T_c. The CDW wave vector, $q_0(T)$, shows a nonmonotonic dependence on temperature (Fig. 2*D*). This behavior has also been observed in X-ray measurements of other tritellurides (19) and is a common characteristic of incommensurate CDWs. The exact value of q_0 reflects a balance between Fermi surface morphology, lattice pinning, the compressibility of uncondensed electrons, and coupling to other order parameters (49–51). The behavior of $q_0(T)$ suggests that the CDW in $ErTe_3$ is shaped by a combination of these effects.

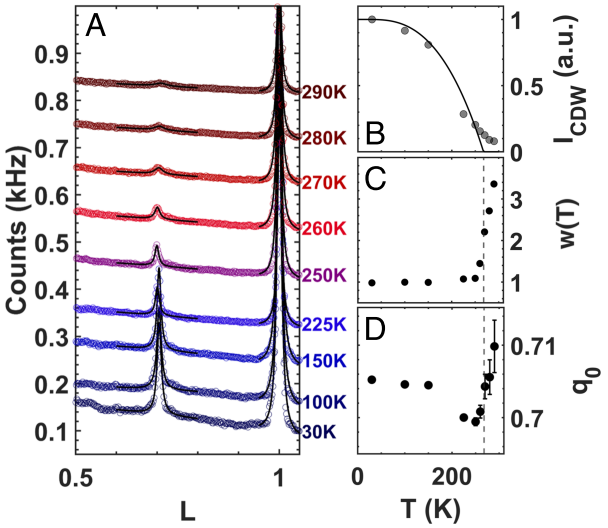

Fig. 2. Elastic scattering: (*A*) M-EELS spectra ($\omega \approx 0$) as a function of q for different temperatures. The solid black lines show the fits to the spectra using Eq. **3**. (*B*) The integrated area under the CDW peak $q \approx q_0$ obtained from fits to Eq. **3** along with a fit to the BCS interpolation formula, normalized to the value in the $T \to 0$ limit. (*C*) $w(T) = \gamma_{CDW}/\gamma_{(0,1)}$, the ratio of the width of the CDW satellite to that of the Bragg peak, plotted as a function of temperature. (*D*) Ordering wave vector q_0 plotted as a function of temperature. The vertical gray dashed line in (*C* and *D*) denotes the T_c obtained from the fit in (*B*).

Having established the structural properties of the CDW through elastic scattering, we now focus on its collective dynamics. Fig. 3 *A* and *B* present the temperature dependence of the M-EELS spectra at $q = 0.6$ r.l.u. and near the CDW ordering wave vector, $q = q_0$. At all temperatures and momenta, the spectra are dominated by a quasielastic response, with no evidence of dispersive collective excitations. This finding contrasts sharply with IXS studies, which reveal a softening of phonon modes near the CDW wave vector above T_{C1} (25, 26). Since M-EELS is more sensitive to valence band electronic excitations, while IXS primarily detects phonons, this suggests that the electronic excitations in $ErTe_3$ behave quite differently from its lattice excitations. This conclusion is further reinforced by the absence of phonon peaks in the low-energy optical conductivity of $ErTe_3$ (22), an effect attributed to strong metallic screening.

Despite the absence of well-defined, propagating collective modes, the dynamical charge susceptibility shows a pronounced temperature dependence. A broadening of the quasielastic response is evident in the raw spectrum (Fig. 3 *A* and *B*), suggesting that the CDW undergoes nontrivial, relaxational dynamics at an energy scale of $\sim k_B T$.

We parameterized this relaxational behavior using the Glauber model [also known as "model A" (52)], which describes the diffusive dynamics of a nonconserved scalar order parameter. In this model, the imaginary part of the susceptibility, $\chi''(q, \omega, T)$, is given by

$$\chi''(q, \omega, T) = A(q, T)\frac{\omega}{\omega^2 + \gamma^2(q, T)}, \quad [4]$$

where ω represents the frequency, $\gamma(q, T)$ is the relaxation rate that captures the diffusive dynamics, and $A(q, T)$ sets the overall scale. We fit the M-EELS response using the expression

$$I(q, \omega, T) = V_{\text{eff}}^2(\omega, q)\, n(\omega, T)\, \chi''(\omega, q, T), \quad [5]$$

where $n(\omega, T)$ is the Bose occupation factor and $V_{\text{eff}}(\omega, q)$ is the Coulomb matrix element (32). This minimal model, with only two adjustable parameters (A and γ) provides excellent fits to the M-EELS data (*SI Appendix*), confirming that the charge dynamics in $ErTe_3$ are predominantly relaxational.

The behavior of the relaxation rate in the vicinity of the CDW is summarized in Fig. 3*C*, which shows $\gamma(q, T)$ as a function of q for different temperatures. A pronounced minimum is observed near q_0, reflecting a prominent energy narrowing of the quasielastic line. This indicates critical slowing down of the CDW fluctuations near q_0 in the vicinity of the transition temperature. While this behavior is expected near a second-order phase transition, the scattering rate remains temperature-dependent across all momenta—even far from the CDW wave

vector, q_0. This observation indicates that density fluctuations are present at all temperatures and length scales, beyond the conventional CDW fluctuations expected near q_0.

However, the temperature dependence of the scattering rate differs significantly near the CDW wave vector compared to the rest of the Brillouin zone, as shown in Fig. 3*D*. At $q = 0.6$, the scattering rate decreases monotonically with temperature, resembling the behavior of the resistivity observed in transport experiments (19). In contrast, near $q \sim q_0$, the scattering rate drops sharply as the sample is cooled through the CDW phase transition, then decreases more gradually as the temperature is further lowered deep into the ordered phase.

For momenta near the CDW ordering wave vector, the scattering rate has a roughly parabolic dependence on q. As a result, the CDW dynamics can be described by a diffusion model:

$$\gamma(q, T) = \hbar\tau^{-1} + \hbar D(T)\,(q - q_0)^2, \qquad [6]$$

where τ^{-1} represents pure dissipation and $D(T)$ is the diffusion constant. Fig. 3 *E* and *F* show plots of τ^{-1} and $D(T)$, respectively. The dissipation rate, τ^{-1}, varies quadratically with temperature, consistent with the behavior of a good Fermi liquid. Intriguingly, $D(T)$ peaks around ~250 K, slightly below T_C where a strong violation of the Wiedemann–Franz law was previously observed in thermal transport measurements (53). This suggests that electronic CDW excitations propagate diffusively, with the diffusivity reaching its maximum just below T_C, when the CDW amplitude is large but still subject to significant thermal fluctuations. The characteristic diffusion length, λ, defined as $\lambda \sim \sqrt{D\,\tau}$, ranges between ~2 to 10 lattice constants, comparable to that observed in the "stripe-ordered" phase $La_{2-x}Ba_xCuO_4$ $\left(x \sim \frac{1}{8}\right)$ with time-resolved X-ray scattering experiments (54).

Finally, our analysis allows us to quantify the behavior of the static susceptibility, $\chi(q, T)$, which is traditionally expected to diverge near a CDW transition (1). The static susceptibility is given by the real part of the complex susceptibility $\chi(q, \omega)$ evaluated at zero frequency. While this could be obtained via a Kramers–Kronig transformation of the data, we can also directly compute it from the real part associated with Eq. **4**,

$$\chi'(q, \omega, T)|_{\omega=0} = A(q, T)/\gamma(q, T). \qquad [7]$$

Fig. 4*A* presents this static susceptibility as a function of q at various temperatures, normalized to $\chi'(q, 0, 290\,K)$. A peak is observed near q_0, which sharpens and increases in magnitude as the temperature decreases, suggesting a divergence associated with CDW formation. While such a peak is theoretically expected, this represents to the best of our knowledge, the first experimental observation of this phenomenon.

Fig. 4*A* reveals a surprising result: while the static susceptibility peaks at q_0, as expected for the CDW, it does not diverge at T_{C1} (*SI Appendix*, Fig. S4*J*). Instead, it continues to increase down to the lowest measured temperature, suggesting a divergence at $T \sim 0$. This behavior aligns with the expectations for the unrenormalized susceptibility (1). However, M-EELS is an experiment, and therefore—by definition—measures the fully renormalized susceptibility for all the electrons, which should exhibit a divergence at T_{C1} (1).

Despite this, a thermodynamic signature is not entirely absent. In Fig. 4*B*, we plot the momentum-integrated intensity of the CDW as a function of temperature, separately showing the peak and the background. While the background evolves smoothly, the integrated intensity of the peak exhibits a slight singularity at $T = T_{C1}$. Thus, the transition does show an anomaly, though it is much less pronounced than one might expect.

A possible explanation for this behavior is that only a small fraction of electrons at the Fermi surface participate in the CDW

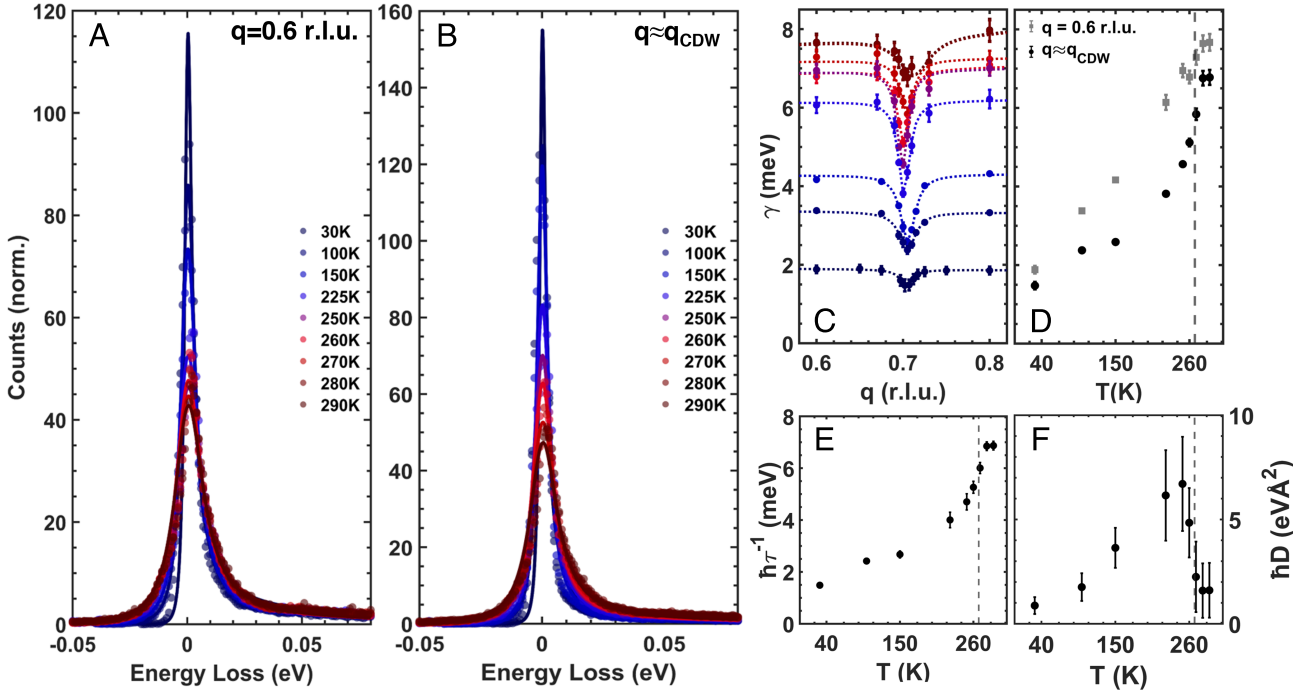

Fig. 3. Dynamical response: Low energy M-EELS spectra, normalized to constant spectral weight, for different temperatures for (*A*) $q = 0.6$ (r.l.u.) and (*B*) $q \sim q_0$. The solid lines show the fits to the data using Eq. **5**. (*C*) $\gamma(q, T)$ extracted by fitting the loss spectra to Eq. **5**. The dashed lines are a guide to the eye. (*D*) Temperature dependence of $\gamma(q, T)$ for $q = 0.6$ (r.l.u.) and $q \approx q_0$. (*E*) τ^{-1} and (*F*) D obtained from fitting $\gamma(q, T)$ near q_0 to Eq. **6**.

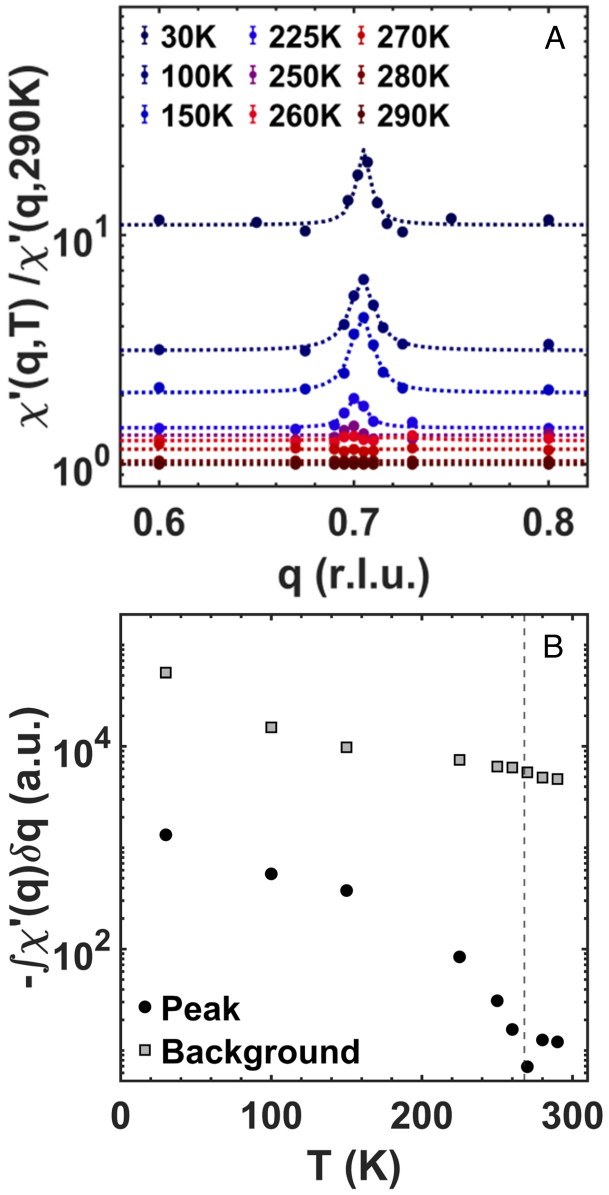

Fig. 4. Singular behavior of the charge susceptibility: (*A*) Real part of the charge susceptibility $\chi'(q,\omega = 0,t)$ extracted from Eq. **7** normalized to its value at $T = 290$ K. The dashed lines are a guide to the eye. (*B*) Temperature dependence of $\int \chi'(q,\omega = 0)dq$, showing the contributions from the Lorentzian CDW peak and the linear background.

order. In this case, the bare and renormalized susceptibilities would be very similar. This scenario is supported by ARPES measurements (20), which indicate that the CDW gap appears only on a limited portion of the Fermi surface, as well as by transport studies showing that $ErTe_3$ remains metallic even in the ordered phase (19).

Alternatively, the transition may be influenced by disorder. Evidence for disorder effects can be seen in Fig. 2*A*, where the CDW momentum spectrum exhibits a Lorentzian lineshape, and in Fig. 2*B*, which shows a slightly rounded transition. By broadening the transition, disorder can smear out any sharp thermodynamic anomaly associated with the CDW.

Finally, we note that, while the largest changes in the static susceptibility occur at q_0, the susceptibility shows significant temperature dependence at all momenta measured, which appear as a linear background in Eq. **3**. This indicates that a substantial fraction of the valence electrons—even those not directly involved in CDW ordering—contribute significantly to the overall change in charge susceptibility. What underlying physics would drive such fluctuations everywhere in momentum space is an open question.

Materials and Methods

Single crystal samples of $ErTe_3$, approximately 1.5 × 2.5 × 0.5 mm in size were grown using the self-flux method. Additional details on the crystal growth process can be found in ref. 16. The material naturally grows with the large [010] facets with the b-axis perpendicular to the basal plane. The crystalline facets were clearly observable under an optical microscope.

Prior to the M-EELS measurements, the samples were mounted on OFHC copper pucks using Ag-epoxy (EPOTEK H20-E) and custom aluminum posts were mounted on top of the samples. The epoxy was cured at 140 °C for 45 min under steady ultra-high-purity (99.999%) nitrogen flow to prevent oxidation. The prepared samples were loaded into a UHV chamber under $\sim 1.2 \times 10^{-10}$ Torr vacuum and mechanically cleaved at room temperature. Subsequently the samples were transferred to the M-EELS measurement chamber which was held at $\sim 7 \times 10^{-11}$ torr vacuum or better for the remainder of the experiment.

M-EELS experiments were conducted using a modified high-resolution EELS spectrometer (ELS5000, LK Technologies) with the sample placed in an eucentric cryogenic three-circle goniometer (see ref. 32 for further details). The sample was aligned such that the in-plane momentum transfer was along the c-axis. Incident beam energy was set to 50 eV, and the energy resolution, measured on the direct beam, was ∼5.6 meV. The effective momentum resolution (in the scattering plane) was ~ 0.02 Å^{-1} (55) and includes contribution from both the beam parameters and the cleaved surface quality.

Subsequent analysis of the momentum scans at $\omega = 0$, and energy loss scans at constant q were performed using the procedure described in the main text and *SI Appendix*. The raw data, along with the details of the fitting models and outputs are included in *SI Appendix*.

Data, Materials, and Software Availability. All study data are included in the article and/or *SI Appendix*.

ACKNOWLEDGMENTS. We thank Steven A. Kivelson and Anisha G. Singh for helpful discussions. momentum-resolved electron energy loss spectroscopy (M-EELS) measurements were supported by the Center for Quantum Sensing and Quantum Materials, an Energy Frontier Research Center funded by the US Department of Energy (DOE), Office of Science, Basic Energy Sciences (BES), under award DE-SC0021238. Q.J. and I.R.F. (crystal growth and characterization) were supported by DOE BES contract DE-AC02-76SF00515. T.-C.C. (surface preparation) was supported by DOE BES contract DE-FG02-07ER46383. E.F. (theory) was supported by NSF grant DMR 2225920. Q.J. was also partially supported by a Geballe Laboratory for Advanced Materials Postdoctoral Fellowship. P.A. gratefully acknowledges support from the Emergent Phenomena in Quantum Systems Initiative program of the Gordon and Betty Moore Foundation, grant GBMF9452.

Author affiliations: [a]Department of Physics, University of Illinois at Urbana-Champaign, Urbana, IL 61801; [b]Materials Research Laboratory, University of Illinois at Urbana-Champaign, Urbana, IL 61801; [c]Department of Applied Physics, Stanford University, Stanford, CA 94305; and [d]Institute of Condensed Matter Theory, University of Illinois at Urbana-Champaign, Urbana, IL 61801

1. G. Grüner, *Density Waves in Solids* (CRC Press, 2018).
2. S. M. Hayden and J. M. Tranquada, Charge correlations in cuprate superconductors. *Annu. Rev. Condens. Matter Phys.* **15**, 215–235 (2023).
3. J. Hwang *et al.*, Charge density waves in two-dimensional transition metal dichalcogenides. *Rep. Prog. Phys.* **87**, 044502 (2024).
4. D. Jérome, Organic conductors: From charge density wave TTF-TCNQ to superconducting $(TMTSF)_2PF_6$. *Chem. Rev.* **104**, 5565–5592 (2004).
5. G. Grüner, The dynamics of charge-density waves. *Rev. Mod. Phys.* **60**, 1129 (1988).
6. C.-W. Chen, J. Choe, E. Morosan, Charge density waves in strongly correlated electron systems. *Rep. Prog. Phys.* **79**, 084505 (2016).

7. M. D. Johannes, I. I. Mazin, C. A. Howells, Fermi-surface nesting and the origin of the charge-density wave in $NbSe_2$. *Phys. Rev. B Condens. Matter Mater. Phys.* **73**, 205102 (2006).
8. M. D. Johannes, I. I. Mazin, Fermi surface nesting and the origin of charge density waves in metals. *Phys. Rev. B Condens. Matter Mater. Phys.* **77**, 165135 (2008).
9. T. Philipp Aebi, H. B. Pillo, F. Lévy, On the search for fermi surface nesting in quasi-2d materials. *J. Electron Spectrosc. Relat. Phenom.* **117**, 433–449 (2001).
10. K. Rossnagel, On the origin of charge-density waves in select layered transition-metal dichalcogenides. *J. Phys. Condens. Matter* **23**, 213001 (2011).
11. C. M. Varma, A. L. Simons, Strong-coupling theory of charge-density-wave transitions. *Phys. Rev. Lett.* **51**, 138 (1983).
12. H.-M. Eiter *et al*., Alternative route to charge density wave formation in multiband systems. *Proc. Natl. Acad. Sci. U.S.A.* **110**, 64–69 (2013).
13. F. Flicker, J. Van Wezel, Charge order from orbital-dependent coupling evidenced by $NbSe_2$. *Nat. Commun.* **6**, 7034 (2015).
14. R. A. Craven, S. F. Meyer, Specific heat and resistivity near the charge-density-wave phase transitions in 2H-$TaSe_2$ and 2H-TaS_2. *Phys. Rev. B* **16**, 4583 (1977).
15. Z. Z. Wang *et al*., Charge density wave transport in $(TaSe4)_2I$. *Solid State Commun.* **46**, 325–328 (1983).
16. N. Ru, I. R. Fisher, Thermodynamic and transport properties of YTe_3, $LaTe_3$, and $CeTe_3$. *Phys. Rev. B Condens. Matter Mater. Phys.* **73**, 033101 (2006).
17. A. W. Overhauser, Observability of charge-density waves by neutron diffraction. *Phys. Rev. B* **3**, 3173 (1971).
18. J. L. Hodeau *et al*., Charge-density waves in $NbSe_3$ at 145K: Crystal structures, X-ray and electron diffraction studies. *J. Phys. C Solid State Phys.* **11**, 4117 (1978).
19. N. Ru *et al*., Effect of chemical pressure on the charge density wave transition in rare-earth tritellurides RTe_3. *Phys. Rev. B Condens. Matter Mater. Phys.* **77**, 035114 (2008).
20. R. G. Moore *et al*., Fermi surface evolution across multiple charge density wave transitions in $ErTe_3$. *Phys. Rev. B Condens. Matter Mater. Phys.* **81**, 073102 (2010).
21. F. Clerc *et al*., Fermi surface of layered compounds and bulk charge density wave systems. *J. Phys. Condens. Matter* **19**, 355002 (2007).
22. B. F. Hu *et al*., Optical study of the multiple charge-density-wave transitions in $ErTe_3$. *Phys. Rev. B Condens. Matter Mater. Phys.* **84**, 155132 (2011).
23. L. Degiorgi, B. Alavi, G. Mihály, G. Grüner, Complete excitation spectrum of charge-density waves: Optical experiments on $K_{0.3}MoO_3$. *Phys. Rev. B* **44**, 7808 (1991).
24. A. Perucchi, L. Degiorgi, R. E. Thorne, Optical investigation of the charge-density-wave phase transitions in $NbSe_3$. *Phys. Rev. B* **69**, 195114 (2004).
25. M. Maschek *et al*., Wave-vector-dependent electron-phonon coupling and the charge-density-wave transition in $TbTe_3$. *Phys. Rev. B* **91**, 235146 (2015).
26. M. Maschek *et al*., Competing soft phonon modes at the charge-density-wave transitions in $DyTe_3$. *Phys. Rev. B* **98**, 094304 (2018).
27. A. Q. R. Baron, "High-resolution inelastic x-ray scattering I: Context, spectrometers, samples, and superconductors" in *Synchrotron Light Sources and Free-Electron Lasers: Accelerator Physics, Instrumentation and Science Applications*, E. J. Jaeschke, S. Khan, J. R. Schneider, J. B. Hastings, Eds. (Springer Nature, 2020), pp. 2131–2212.
28. D. E. Moncton, J. D. Axe, F. J. DiSalvo, Neutron scattering study of the charge-density wave transitions in 2H-$TaSe_2$ and 2H-$NbSe_2$. *Phys. Rev. B* **16**, 801 (1977).
29. M. Sato, H. Fujishita, S. Sato, S. Hoshino, Neutron inelastic scattering and x-ray structural study of the charge-density-wave state in $K_{0.3}MoO_3$. *J. Phys. C Solid State Phys.* **18**, 2603 (1985).
30. E. Balcar, S. W. Lovesey, *Theory of Magnetic Neutron and Photon Scattering* (Clarendon Press, Oxford, 1989).
31. A. T. Boothroyd, *Principles of Neutron Scattering from Condensed Matter* (Oxford University Press, U.K., 2020).
32. S. Vig *et al*., Measurement of the dynamic charge response of materials using low-energy, momentum-resolved electron energy-loss spectroscopy (M-EELS). *SciPost Phys.* **3**, 026 (2017).
33. P. Abbamonte, J. Fink, Collective charge excitations studied by electron energy-loss spectroscopy. *Annu. Rev. Condens. Matter Phys.* **16**, 465–480 (2025).
34. J. Laverock *et al*., k-resolved susceptibility function of 2 H-TaSe 2 from angle-resolved photoemission. *Phys. Rev. B-Condens. Matter Mater. Phys.* **88**, 035108 (2013).
35. H. Ibach, D. L. Mills, *Electron Energy Loss Spectroscopy and Surface Vibrations* (Academic press, 2013).
36. A. Kogar *et al*., Surface collective modes in the topological insulators Bi_2Se_3 and $Bi_{0.5}Sb_{1.5}Te_{3-x}Se_x$. *Phys. Rev. Lett.* **115**, 257402 (2015).
37. A. Kogar *et al*., Signatures of exciton condensation in a transition metal dichalcogenide. *Science* **358**, 1314–1317 (2017).
38. M. Mitrano *et al*., Anomalous density fluctuations in a strange metal. *Proc. Natl. Acad. Sci. U.S.A.* **115**, 5392–5396 (2018).
39. A. A. Husain *et al*., Crossover of charge fluctuations across the strange metal phase diagram. *Phys. Rev. X* **9**, 041062 (2019).
40. S. Xue *et al*., Observation of nodal-line plasmons in ZrSiS. *Phys. Rev. Lett.* **127**, 186802 (2021).
41. A. A. Husain *et al*., demon observed as a 3D acoustic plasmon in Sr_2RuO_4. *Nature* **621**, 66–70 (2023).
42. C. S. Kengle *et al*., Non-RPA behavior of the valence plasmon in $SrTi_{1-x}Nb_xO_3$. *Phys. Rev. B* **108**, 205102 (2023).
43. K. Yumigeta *et al*., Advances in rare-earth tritelluride quantum materials: Structure, properties, and synthesis. *Adv. Sci.* **8**, 2004762 (2021).
44. J. A. W. Straquadine, M. S. Ikeda, I. R. Fisher, Evidence for realignment of the charge density wave state in $ErTe_3$ and $TmTe_3$ under uniaxial stress via elastocaloric and elastoresistivity measurements. *Phys. Rev. X* **12**, 021046 (2022).
45. H. Yao, J. A. Robertson, E.-A. Kim, S. A. Kivelson, Theory of stripes in quasi-two-dimensional rare-earth tellurides. *Phys. Rev. B Condens. Matter Mater. Phys.* **74**, 245126 (2006).
46. M. Holt, P. Zschack, H. Hong, C. Y. Chou, T. C. Chiang, X-ray studies of phonon softening in $TiSe_2$. *Phys. Rev. Lett.* **86**, 3799–3802 (2001).
47. Y. Imry, S.-K. Ma, Random-field instability of the ordered state of continuous symmetry. *Phys. Rev. Lett.* **35**, 1399–1401 (1975).
48. L. Nie, G. Tarjus, S. A. Kivelson, Quenched disorder and vestigial nematicity in the Pseudogap regime of the cuprates. *Proc. Natl. Acad. Sci. U.S.A.* **111**, 7980–7985 (2014).
49. S. Lee *et al*. Generic character of charge and spin density waves in superconducting cuprates. *Proc. Natl. Acad. Sci. U.S.A.*, **119**, e2119429119 (2022).
50. W. L. McMillan, Landau theory of charge-density waves in transition-metal dichalcogenides. *Phys. Rev. B* **12**, 1187–1196 (1975).
51. W. L. McMillan, Theory of discommensurations and the commensurate-incommensurate charge-density-wave phase transition. *Phys. Rev. B* **14**, 1496–1502 (1976).
52. P. M. Chaikin, T. C. Lubensky, and T. A. Witten. *Principles of condensed matter physics* (Cambridge university press Cambridge, 1995), vol. 10.
53. E. D. Kountz *et al*., Anomalous thermal transport and strong violation of Wiedemann-Franz law in the critical regime of a charge density wave transition. *Phys. Rev. B* **104**, L241109 (2021).
54. M. Mitrano *et al*., Ultrafast time-resolved x-ray scattering reveals diffusive charge order dynamics in $La_{2-x}Ba_xCuO_4$. *Sci. Adv.* **5**, eaax3346 (2019).
55. J. Chen *et al*., Consistency between reflection momentum-resolved electron energy loss spectroscopy and optical spectroscopy measurements of the long-wavelength density response of $Bi_2Sr_2CaCu_2O_{8+x}$. *Phys. Rev. B* **109**, 045108 (2024).

PNAS

Supporting Information for - Measurement of the dynamic charge susceptibility near the charge density wave transition in $ErTe_3$

Dipanjan Chaudhuri[1], Qianni Jiang, Xuefei Guo, Jin Chen, Caitlin S. Kengle, Farzaneh Hoveyda-Marashi, Camille Bernal-Choban, Niels de Vries, Tai-Chang Chiang, Eduardo Fradkin, Ian R. Fisher, Peter Abbamonte[2]

E-mail: [1] dc36@illinois.edu [2] abbamont@illinois.edu

The supplemental materials contains detailed fits to the static and the dynamical response discussed in the main text. The fits were obtained using the nonlinear least-squares solver in Matlab.

1. M-EELS scattering cross-section

M-EELS is an inelastic electron scattering experiment that combines high-resolution EELS (HREELS) with triple-axis alignment techniques from x-ray and neutron scattering and directly measures the imaginary part of the frequency- and wavevector-dependent density response function, $\chi''(q,\omega,T)$. The generalized M-EELS cross section can be derived using the distorted-wave Born approximation (DWBA) method, outlined previously in Refs. (1, 2), and is given by the equation:

$$\frac{\partial^2\sigma}{\partial\Omega\partial E} = \sigma_0 V_{\text{eff}}^2(\mathbf{q}) \int_{-\infty}^{0} dz_1 dz_2 e^{-|\mathbf{q}||z_1+z_2|} \cdot S(\mathbf{q}, z_1, z_2, \omega), \quad [1]$$

where $V_{\text{eff}}(\mathbf{q}) = \dfrac{e^2/\epsilon_0}{q^2 + \left(k_i^z + k_s^z\right)^2}$, is an effective Coulomb propagator that describes the interaction between the probe electron and the excitations near the surface of the semi-infinite system (Coulomb matrix element). The integral in Eq. (1) is connected to the density-density correlation function of the surface, defined as

$$S_S(\mathbf{q},\omega) = \int_{-\infty}^{0} dz_1 dz_2 e^{-|\mathbf{q}||z_1+z_2|} S(\mathbf{q}, z_1, z_2, \omega) \approx S(\mathbf{q}, 0, 0, \omega). \quad [2]$$

The surface response function is related to the density correlation function via the quantum mechanical version of the fluctuation-dissipation theorem,

$$S_S(\mathbf{q},\omega) = -\frac{1}{\pi}\frac{1}{1-e^{-\hbar\omega/k_BT}}\chi_S''(\mathbf{q},\omega), \quad [3]$$

where $\chi_S''(\mathbf{q},\omega)$ is the imaginary part of the density response function of the surface, $[-\pi(1-e^{-\hbar\omega/k_BT})]^{-1} = n(\omega)$ is the Bose occupation factor that accounts for the the quantum statistics of the bosonic excitations. While this quantity is not precisely the same as the bulk $\chi(\mathbf{q},\omega)$, it has an effective probe depth is $\sim 1/|\mathbf{q}|$, which is typically a few tens of nm or less. This has been validated recently through quantitative agreement between M-EELS and the bulk infrared spectra in a layered material where the former can be computed from the latter (3). Thus, within the Born approximation, M-EELS directly measures the dynamic charge susceptibility.

2. Sensitivity of IXS and EELS to phonon excitations

In the main manuscript, we assert that EELS techniques are primarily sensitive to valence band electronic excitations, whereas non-resonant IXS is more sensitive to phonons. The underlying reasons for this distinction have been discussed previously (1), but we provide a brief review here.

EELS measures the dynamic charge susceptibility of the system,

$$\chi_\rho(r,t,r',t') = \frac{-i}{\hbar}\left\langle[\hat\rho(r,t),\hat\rho(r,t)]\right\rangle\theta(t-t'), \quad [4]$$

where $\hat\rho(r,t)$ is the total charge density operator (1, 4). As a result, EELS directly probes collective charge dynamics, with its sensitivity to different excitations determined by how strongly they modulate the charge density. In a three-dimensional homogeneous system, collective charge modes can be identified as poles in the complex Fourier transform of Eq. 4, $\chi_\rho(q,\omega)$.

By contrast, non-resonant inelastic X-ray scattering (IXS) measures a related but distinct quantity (5),

$$\chi_n(r,t,r',t') = \frac{-i}{\hbar}\left\langle[\hat n(r,t),\hat n(r,t)]\right\rangle\theta(t-t'), \quad [5]$$

where $\hat n(r,t)$ represents the total electron density operator. The key difference between $\hat\rho(r,t)$ and $\hat n(r,t)$ is that $\hat\rho(r,t)$ accounts for all charges in the system, including both electrons and nuclei, whereas $\hat n(r,t)$ includes only the electronic contribution. In most cases, nuclear charges have negligible impact on x-ray scattering measurements.

The distinction between $\hat\rho(r,t)$ and $\hat n(r,t)$ implies a difference in the way EELS and IXS weight different kinds of excitations. In IXS, excitations are weighted based on the extent to which they modulate the *electron* density. In most solids, the majority

of electrons reside in core states bound to nuclei, meaning excitations that displace atomic cores—i.e., phonons—produce the strongest modulation of electron density. As a result, phonons appear with disproportionately high intensity in IXS spectra, while electronic excitations are comparatively weaker. This is the reason many researchers have turned to resonant IXS (RIXS) techniques, which provides enhances sensitivity to valence band excitations.

By contrast, phonons and electronic excitations appear in EELS measurements in a more balanced way, providing similar valence band sensitivity to RIXS approaches.

3. Elastic response

The Bragg peak and the CDW satellite at each temperature are fit to a Lorentzian form with a linear background given by,

$$I(q,T) = \frac{A(T)}{(q-q_0(T))^2 + \gamma_q^2(T)} + m(T)q + c(T) \quad [6]$$

where $q_0(T)$ is the center frequency ($q_0 \sim 0.7$ for CDW, $q_0 \approx 1$ for Bragg peak) and $\gamma_q(T)$ is the width. Lorentzian fits to the Bragg peak [Fig. S1(a)] are motivated by previous x-ray scattering experiments (6, 7). As discussed in the main text, we found that the momentum-lineshape of the CDW satellites could be fit to a single-Lorentzian lineshape [Fig. S1(b)]. Furthermore, in Fig. S1(c), we show fits to the expression suggested by Nie and coworkers (8, 9) for disordered systems (with a linear background), which is given by

$$S(Q,T) = \sigma^2 G^2(Q,T) + TG(Q,T) + m(T)q + c(T) \quad [7]$$

where $G(Q,T) = 1/[\kappa Q^2 + \mu(T)]$ is a Lorentzian, $Q = q - q_0$ is the momentum relative to the CDW wave vector, $\mu(T)$ is related to the CDW correlation length, σ and κ are temperature independent parameters that represent the disorder strength and CDW stiffness. We quantify the goodness of fit using chi-squared test statistic using the expression,

$$X^2 = \sum \frac{(I_{exp} - I_{fit})^2}{I_{fit}} \quad [8]$$

where $I_{exp/fit}$ represent the experimental and fitted intensities respectively. Using this metric, we performed a global fit of the elastic response to Eq. (7) at all temperatures and found the minima at $\sigma = 2.6$ and $\kappa = 2500$. Nevertheless, we observed that the fits were comparable to that obtained using Eq. (6) with lesser number of fit parameters. Hence, we conclude that the impact of disorder here is extremely weak.

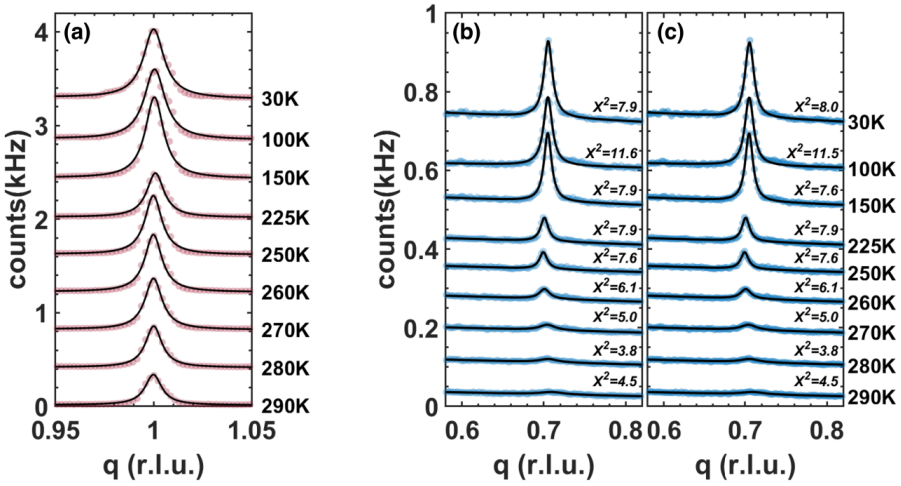

Fig. S1. Fits of the (a) Bragg peaks and (b) CDW satelites at each temperature to Eq. (6). (c) Fits of the CDW satelites at each temperature to Eq. (7). The filled circles denote the data points and solid lines show the fitted curve. The spectra are plotted with vertical offset (0.4 for Bragg peaks, 0.075 for CDW) for clarity.

4. Dynamic response

As described in section 1, the ineM-EELS response can be modeled using the expression

$$I(q,\omega,T) = V_{\text{eff}}^2(\omega,q)n(\omega,T)\chi''(\omega,q,T). \quad [9]$$

Here $n(\omega,T)$ is the Bose occupation factor, and $V_{\text{eff}}(\omega,q)$ is the matrix element. We use Glauber model for the dynamic charge susceptibility where the imaginary part, $\chi''(q,\omega,T)$, is given by

$$\chi''(q,\omega,T) = A(q,T)\frac{\omega}{\omega^2 + \gamma^2(q,T)} \quad [10]$$

where $\gamma(q,T)$ is a scattering rate that captures the diffusive dynamics and $A(q,T)$ is an overall scale factor which is related to the real part of the charge susceptibility, $\chi'(q,\omega,T)$. The fits are shown in fig. S2.

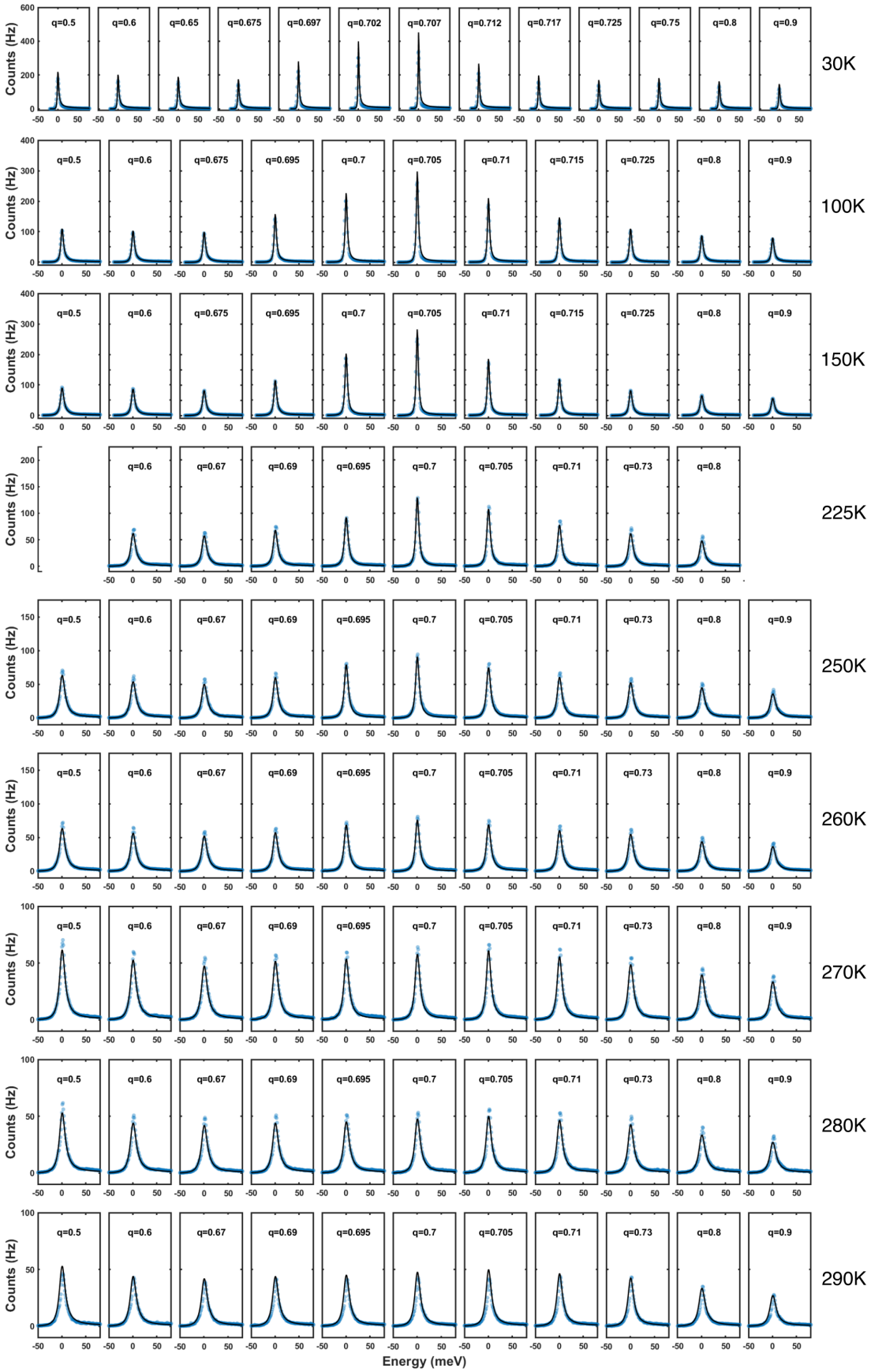

Fig. S2. Fits to the energy loss spectra at each temperature and momentum to Eq. (9). The dots denote the data and solid lines show the fitted curve.

5. Scattering rate

The momentum dependence of the scattering rate locally near the CDW ordering wavevector, can be approximated by a parabolic form based on simple diffusion model as

$$\gamma(q,T) = \hbar\tau^{-1} + \hbar D(T)(q-q_0)^2 \qquad [11]$$

where τ^{-1} describes pure dissipation and $D(T)$ is the diffusion constant. The fits are showed in Fig. S3(a). Temperature dependence of the characteristic diffusion length, $\lambda \sim \sqrt{D\,\tau}$, and site-to-site hopping rate, $\Gamma_{hop} = a^{-1}\sqrt{D/\tau}$ are shown in Fig. S3(b) and Fig. S3(c) respectively.

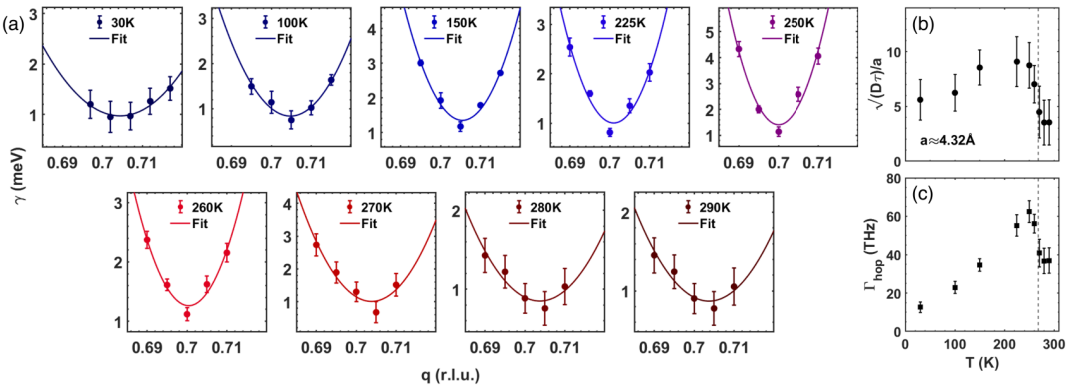

Fig. S3. (a) Fits of the scattering rate extracted from the energy loss spectra to Eq. (11) locally near the CDW wavevector. The dots denote the data and solid lines show the fitted curve. (b) Temperature dependence of the diffusion length λ divided by the lattice constant. (c) Site-to-site hopping rate calculated from combining the decay rate, diffusion constant, and lattice parameter.

6. Fits to $\chi'(q,\omega=0,T)$

As discussed in the main text, the momentum dependence of real part of the static susceptibility, $\chi'(q,\omega=0,T)$, can be obtained through the ratio $A(q,T)/\gamma(q,T)$. This can also be modeled using a Lorentzian and a linear background given by Eq. (6)). Fig. S4 (a-i) shows these fits for different temperature. The area under the Lorentzian peak shows a slight discontinuity at the T_C as shown in the main text Fig. 4(b) while the background evolves smoothly through T_C. The peak value of static susceptibility at at q_0 evolves smoothly through T_C and appears to diverge at the lowest temperature, shown in Fig. S4 (j).

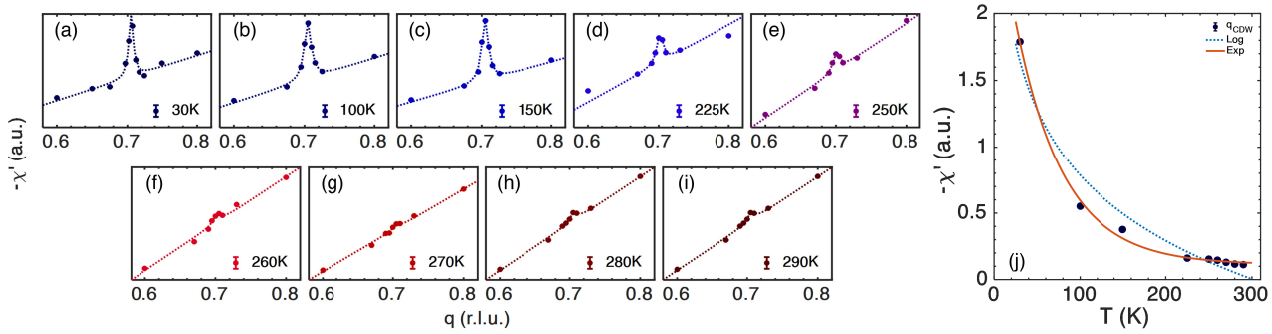

Fig. S4. (a-1) Fits to $\chi'(q,\omega=0,T)$. The dots denote the data and solid lines show the fitted curve. (j) Temperature dependence of $\chi'(q,\omega=0,T)$, together with logarithmic and exponential fits.

Dipanjan Chaudhuri[1], Qianni Jiang, Xuefei Guo, Jin Chen, Caitlin S. Kengle, Farzaneh Hoveyda-Marashi, Camille Bernal-Choban, Niels de Vries, Tai-Chang Chiang, Eduardo Fradkin, Ian R. Fisher, Peter Abbamonte[2]

References

1. S Vig, et al., Measurement of the dynamic charge response of materials using low-energy, momentum-resolved electron energy-loss spectroscopy (M-EELS). *SciPost Phys.* **3**, 026 (2017).
2. H Ibach, DL Mills, *Electron energy loss spectroscopy and surface vibrations*. (Academic press), (2013).
3. J Chen, et al., Consistency between reflection momentum-resolved electron energy loss spectroscopy and optical spectroscopy measurements of the long-wavelength density response of $Bi_2Sr_2CaCu_2O_{8+x}$. *Phys. Rev. B* **109**, 045108 (2024).
4. P Abbamonte, J Fink, Collective charge excitations studied by electron energy-loss spectroscopy. *Annu. Rev. Condens. Matter Phys.* **16**, 465–480 (2025).
5. W Schülke, U Bonse, H Nagasawa, S Mourikis, A Kaprolat, Lattice-induced double peak in the dielectric response of be metal. *PRL* **59**, 1361 (1987).
6. P Heiney, P Stephens, R Birgeneau, P Horn, D Moncton, X-ray scattering study of the structure and freezing transition of monolayer xenon on graphite. *Phys. Rev. B* **28**, 6416 (1983).
7. PW Stephens, et al., High-resolution x-ray-scattering study of the commensurate-incommensurate transition of monolayer Kr on graphite. *Phys. Rev. B* **29**, 3512 (1984).
8. L Nie, G Tarjus, SA Kivelson, Quenched disorder and vestigial nematicity in the pseudogap regime of the cuprates. *Proc. Natl. Acad. Sci.* **111**, 7980–7985 (2014).
9. S Lee, et al., Generic character of charge and spin density waves in superconducting cuprates. *Proc. Natl. Acad. Sci.* **119**, e2119429119 (2022).